Chapter 4

Nanolevel Surface Processing of Fine Particles by Waterjet Cavitation and Multifunction Cavitation to Improve the Photocatalytic Properties of Titanium Oxide

Toshihiko Yoshimura, Kumiko Tanaka and Masataka Ijiri

Additional information is available at the end of the chapter

http://dx.doi.org/10.5772/intechopen.79530

Abstract

Titanium oxide particles were treated by water jet cavitation (WJC) generated and multifunction cavitation (MFC) using an ejector nozzle. Generation, growth, and collapse of cavitation are repeated with the particles of titanium oxide and platinum. Because the cavitation has an extremely high collapse pressure, the surface of the titanium oxide particles is processed by the microjets of cavitation in a reactor comprising the ejector nozzle. In the multifunction cavitation, ultrasonic irradiation of a waterjet during floating cavitation was used to generate microjets with hot spots. Hot working can be performed at the nanoscale on a material surface using this MFC process, resulting in morphological changes and variations in the surface electrochemical characteristics. The fundamental characteristics of multifunction cavitation were investigated theoretically and experimentally. Furthermore, the additional nozzle was put on the ejector nozzle in order to increase the temperature and pressure of bubble and the mechanism was clarified. The quantities of hydrogen and oxygen generated from titanium dioxide particles treated by multifunction cavitation in response to UV and visible light irradiation were remarkably increased compared to the amounts produced by particles treated by WJC processing. In this chapter, the methods and their results of processing particles by cavitation are introduced.

Keywords: waterjet cavitation, multifunction cavitation, fine particles, microjets

1. Introduction

In recent years, a variety of industrial applications have been identified for cavitation processing, including peening, surface and molecular structure modifications, fatigue strength improvement, and surface cleaning. Waterjet cavitation involves imparting mechanical action to the surface of a material as the result of the extremely high pressures generated during the collapse of a microjet close to the surface [1]. In contrast, ultrasonic cavitation is known to generate hot spots that can promote chemical reaction by producing temperatures of several thousand K [2]. The authors have developed the multifunction cavitation, which is caused by ultrasonic irradiation of a waterjet during floating cavitation to generate microjets with hot spots. This technique combines the properties of both waterjet and ultrasonic cavitation. Furthermore, the additional nozzle was put on the waterjet nozzle (ejector nozzle) in order to increase the temperature and pressure of bubble. The generation mechanism of ultra-high temperature and pressure cavitation was clarified theoretically. The multifunction cavitation was applied to the enhancement of the photocatalytic properties of titanium oxide under visible light.

At present, there are many technical challenges associated with the development of new energy sources as alternatives to thermal and nuclear power generation. Since the use of hydrogen as a fuel generates only water, hydrogen is seen as a potential clean energy source that does not produce hazardous exhaust gases such as carbon monoxide (CO), hydrocarbons (HCs), or nitrogen oxides (NOx). Hydrogen generation via the decomposition of water using a photocatalyst has been studied extensively, and photocatalytic hydrogen generation under UV irradiation has been developed, typically using titanium oxide as a substrate. Ideally, this technology would exhibit high efficiency in the visible light portion of the electromagnetic spectrum. The study reported herein represents an attempt to move closer to this goal by developing highly efficient, visible light-responsive photocatalyst materials [3].

Titanium oxide (TiO_2) is widely used as a white pigment in paints, UV absorbing materials, and cosmetics. It is both inexpensive and safe, and can even be used as a food additive. In addition, the application of titanium oxide to photoelectrodes and photocatalyst materials with applications in solar energy conversion is also anticipated [4]. The TiO_2 photocatalyst reaction proceeds most efficiently under irradiation by UV light (350 nm). However, only a portion of the sun's emission spectrum is at this wavelength, so it is important for effective energy conversion to be able to use visible light, which comprises one half of the solar energy output. There have been many studies attempting to append other compounds to titanium oxide-based catalysts to obtain visible light responsiveness, but none have successfully produced hydrogen using these catalysts. Previously, we developed a new method for the nanoscale processing of TiO_2 particles as well as a new technique for adding a Pt co-catalyst to TiO_2 particles [5]. Furthermore, TiO_2 particles were processed by multifunction cavitation [6–11] in order to modify the surface morphology and electrochemical surface condition. It was determined that multifunction cavitation is effective at improving the photocatalytic properties of TiO_2 under visible light irradiation.

http://dx.doi.org/10.5772/intechopen.79530

2. Theory of multifunction cavitation and ultra-high temperature and pressure cavitation

2.1. Multifunction cavitation mechanism

Figure 1 shows the mechanism of our multifunction cavitation process, in which ultrasonic radiation is imparted to the cavitation cloud generated by a high pressure waterjet. In this method, the microjets generate mechanical action, but so-called "hot spots [12]" at which chemical reactions can occur are also formed. As the ultrasonic cavitation proceeds, isothermal expansion takes place once the pressure is above the Blake threshold value. Following this expansion, Rayleigh shrinkage occurs. Repeated expansion and shrinkage leads to cavitation, which in turns results in high pressure collapse and the generation of high temperature hot spots. In the conventional heat treatment of metals, the application of heat treatment after cold working is quite different from cold working after heat treatment. In contrast, multifunction cavitation has the capacity to allow so-called microlevel or nanolevel forging, in which the material is simultaneously worked and heat treated.

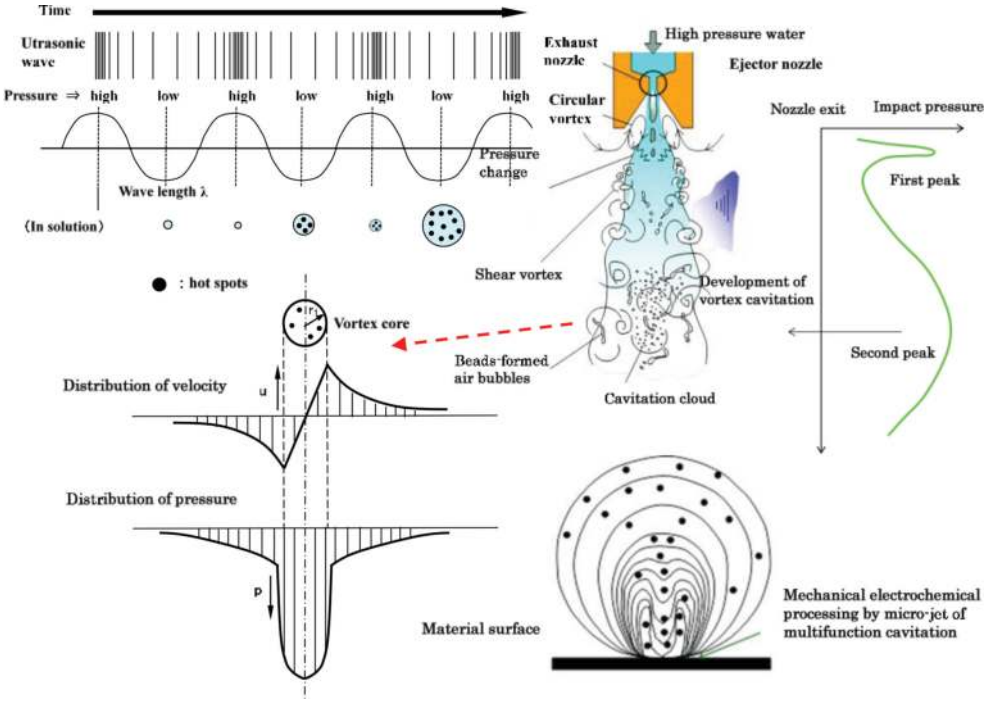

Figure 1. The multifunction cavitation mechanism and mechanical-electrochemical processing by multifunction cavitation microjet.

2.2. Blake threshold

The liquid pressure in the vicinity of the bubble wall, p_B, may be expressed as follows:

$$p_B = \left(p_0 + \frac{2\sigma}{R_0} - p_V\right)\left(\frac{R_0}{R}\right)^{3k} + p_V - \frac{2\sigma}{R} \tag{1}$$

Here, the surface tension, σ, is defined as the surface energy per unit area. In the case of pure water, this value is 7.275 × 10^{-2} (N/m) (J/m^2) at 20°C. The other terms in this equation are the bubble radius R, the equilibrium bubble radius Ro, the static pressure p_0 (normally, 1 atm), and the vapor pressure p_v.

When the heat exchange between the bubble and the surrounding liquid is negligible, thermally insulated conditions can be assumed and $k = \gamma = C_p/C_v$. Here, γ is the heat capacity ratio, equal to the ratio of the molar heat capacity at constant pressure to the molar heat capacity at constant volume (in the case of air, γ = 1.4). When the expansion and the shrinkage of the bubbles is minimal, the process becomes isothermal and k = 1. According to Eq. (1), in the case of an air bubble with Ro = 10 μm in water at 20°C, the minimum value of −0.014 bar occurs at a bubble radius of 30 μm. If the liquid pressure falls below −0.004 bar during the ultrasonic irradiation, the bubble is able to expand greatly.

The minimum value of p_B ($p_{B,min}$) required to expand the bubble can be obtained from Eq. (2):

$$p_{B,\min} = p_v - \frac{4\sigma}{3}\sqrt{\frac{2\sigma}{3R_0^3\left(p_0 + \frac{2\sigma}{R_0} - p_V\right)}} \tag{2}$$

When ultrasonication is applied to the liquid, the liquid pressure at a distance from the bubble wall can be expressed by $p_0 + p_s(t)$. Here, p_0 is the atmospheric pressure and $p_{s(t)}$ is the pressure induced by ultrasonication at time t. The time-dependent term can be expressed as $p_s(t) = A\sin\omega t$, where A is the sound pressure amplitude and ω is the angular frequency. Therefore, the minimum value of $p_{s(t)}$ is −A and the bubble is able to expand at the point at which the value derived from Eq. (2) is equal to $p_0 - A$. This condition can be summarized by the following equation:

$$A_{Blake} = p_0 - p_{B,\min} = p_0 - p_v + \frac{4\sigma}{3}\sqrt{\frac{2\sigma}{3R_0^3\left(p_0 + \frac{2\sigma}{R_0} - p_V\right)}} \tag{3}$$

Thus, the bubble will overcome the effect of surface tension (that is, the Laplace stress) and expand significantly when A ≥ A_{Blake}, where A_{Blake} is the Blake threshold value [13].

In the case that the bubble radius is less than the equilibrium radius, a high sound pressure is necessary to expand the bubble. However, when the bubble radius is greater than the equilibrium radius, the Blake threshold value is approximately equal to atmospheric pressure. Therefore, because the diameters of bubbles being circulated in the waterjet are typically more

than 100 μm, cavitation can readily proceed without the application of especially high sound pressure.

As noted above, the application of ultrasonication during conventional waterjet cavitation (or floating cavitation), generates both high pressure and high temperature cavitation through repeated isothermal expansion and compression under thermally insulated conditions.

2.3. Multifunction cavitation induced by low pressure liquid flow

During the flow of an ideal liquid, the external pressure p_0 in any infinite direction (that is, atmospheric pressure), the pressure p, and the velocity v, are related according to Bernoulli's theorem:

$$\frac{{v_0}^2}{2g} + \frac{p_0}{\gamma} = \frac{v^2}{2g} + \frac{p}{\gamma} \tag{4}$$

Here, g is the acceleration due to gravity and γ is the specific gravity of the liquid. From this relationship, the following equation is derived:

$$p = p_0 + \frac{\rho}{2}\left(v_0^2 - v^2\right) \tag{5}$$

Here, p (or p_v) is the pressure at an arbitrary point and the density of the liquid is expressed by $\rho = \gamma/g$.

As p_0 decreases or v is increased, p is reduced. When the p_v term of Eq. (3) is substituted for the p term in Eq. (5), the following formula is obtained, which expresses the conditions required for cavitation expansion:

$$A_{Blake} = -\frac{\rho}{2}\left(v_0^2 - v^2\right) + \frac{4\sigma}{3}\sqrt{\frac{2\sigma}{3{R_0}^3\left(\frac{2\sigma}{R_0} - \frac{\rho}{2}\left({v_0}^2 - v^2\right)\right)}} \tag{6}$$

The flow rate at a far distance v_0 is zero and the relationship between v and the Blake threshold value is shown in **Figure 2(a)**. The flow rate v is calculated to have a value of 4.52 m/s when the Blake threshold value becomes 1 bar. This result indicates that elevated sound pressure is necessary in order to expand the cavitation at high flow rates.

2.4. Multifunction cavitation induced by liquid flow circulation

Normal waterjet cavitation (or flow cavitation) is typically generated by the application of high pressure waterjets using underwater nozzles. In such cases, the low pressures induced by the whirlpool motion of the fluid result in cavitation.

In the case of a potential flow, the circulation Γ can be defined as follows:

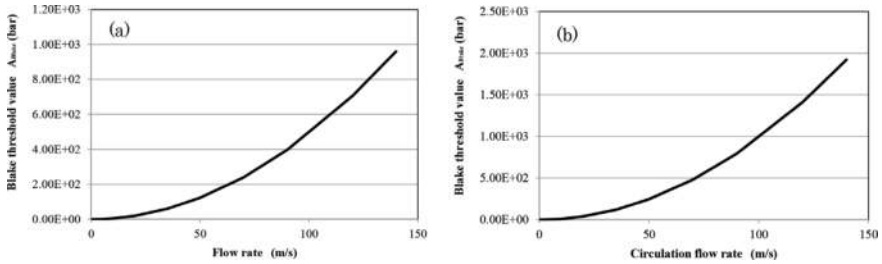

Figure 2. Relationship between the Blake threshold value and the flow rate or the circulation flow rate during waterjet cavitation (a) induced by low pressure liquid flow; (b) induced by circulation generated by liquid flow.

$$2\pi ru = \Gamma \tag{7}$$

This value is not uniform but rather varies with the radius rc from the internal nucleus. The pressure p at a given radius position r_c will be less than the pressure p_1 at a position associated with a wider radius r_1, and may be expressed as follows:

$$p = p_0 - \frac{\rho\Gamma^2}{8\pi^2 {r_1}^4}\left(2{r_1}^2 - {r_c}^2\right) \tag{8}$$

Because r_c = 0 at the nuclear center, the pressure at the center p_m represents the minimum pressure, and may be calculated as in Eq. (9):

$$p_m = p_0 - \frac{\rho\Gamma^2}{4\pi^2 {r_1}^2} \tag{9}$$

When the pressure at the nuclear center, p_m (p_v), equals the saturated steam pressure at the temperature in the region around the flowing water, cavitation will occur. In the case of high pressure waterjets from a nozzle, a circulation whirlpool is formed in the vicinity of the nozzle exit, resulting in flow cavitation. In the case that the equilibrium radius of the air bubble is R_0, and substituting p_m for p_v (the steam pressure) in Eq. (3), the conditions necessary for whirlpool cavitation are achieved, as expressed in the following equation:

$$A_{Blake} = \frac{\rho\Gamma^2}{4\pi^2 {r_1}^2} + \frac{4\sigma}{3}\sqrt{\frac{2\sigma}{3{R_0}^3\left(\frac{2\sigma}{R_0} + \frac{\rho\Gamma^2}{4\pi^2 {r_1}^2}\right)}} \tag{10}$$

At high values of the flow velocity u from the waterjet nozzle, circulation is increased, and when R_0 equals the circulatory nuclear radius r_1, the following equation holds true:

$$A_{Blake} = \frac{\rho\Gamma^2}{4\pi^2 {R_0}^2} + \frac{4\sigma}{3}\sqrt{\frac{2\sigma}{3{R_0}^2\left(2\sigma + \frac{\rho\Gamma^2}{4\pi^2 R_0}\right)}} \tag{11}$$

Assuming circulation of the nuclear radius, the following expression can be written:

$$A_{Blake} = \rho u^2 + \frac{4\sigma}{3}\sqrt{\frac{2\sigma}{3R_0{}^2\left(2\sigma + \frac{\rho\Gamma^2}{4\pi^2 R_0}\right)}} \tag{12}$$

Because the first term on the right hand side of this equation has the greatest effect and the Break threshold increases, significant sound pressure is required to inflate the circulation bubble when the circulation becomes overly large.

Figure 2(b) presents the relationship between u and A_{Blake}. At an A_{Blake} value of 1 bar, the value of u is 3.2 m/s. Under these conditions, high sound pressure is needed to inflate the circulation bubble because the cavitation flow rate in the area of the nozzle exit is more than 100 m/s. These results demonstrate that multifunction cavitation should take place far from the nozzle exit.

As noted, the introduction of ultrasonic irradiation to floating cavitation can result in isothermal expansion. In this technique, the supersonic wave is a primary wave and the pressure pitch repeats with a period of wavelength λ. As an example, in the case of an underwater sound velocity of 500,000 mm/s, λ is 1,500,000 mm/s / 28,000 Hz = 53.6 mm when employing a 28 kHz supersonic wave.

2.5. The Rayleigh-Plesset equation

The expansion and shrinkage of bubbles may be expressed using the Rayleigh-Plesset equation [14, 15] shown below:

$$R\ddot{R} + \frac{3\dot{R}^2}{2} = \frac{1}{\rho}\left(p_g + p_v - \frac{2\sigma}{R} - \frac{4\mu\dot{R}}{R} - p_0 - p_s(t)\right) \tag{13}$$

Here, R is the bubble radius, σ is the surface tension, p_g is the gas pressure, p_0 is the static pressure, p_v is the vapor pressure, and $p_s(t)$ is the sound pressure at time t. The acceleration rate shown below in Eq. (14) can be obtained from Eq. (13).

$$\ddot{R} = -\frac{3\dot{R}^2}{2R} + \frac{1}{\rho R}\left(p_g + p_v - \frac{2\sigma}{R} - \frac{4\mu\dot{R}}{R} - p_0 - p_s(t)\right) \tag{14}$$

When a bubble shrinks severely, such that $\dot{R}^2$ increases, the first term on the right-hand side will be important while the second term can be ignored, and Eq. (15) is obtained:

$$\ddot{R} \approx -\frac{3\dot{R}^2}{2R} \tag{15}$$

The acceleration $\left(\ddot{R}\right)$ of the air bubble wall will always be negative, indicating that the velocity decreases.

When an air bubble shrinks, $\dot{R} < 0$ and this decrease in the shrinkage rate tends to increase the value of $\dot{R}$. That is, the right side of Eq. (15) increases to generate a larger negative value. Therefore, the acceleration rises and there is a more pronounced drop in the velocity. The air bubble shrinkage accelerates automatically and become increasingly large; this is termed Rayleigh shrinkage or Rayleigh collapse.

The air bubble shrinkage continues to accelerate, with gas molecules and steam within the bubble. As such, the pressure in the bubble rises and a portion of the gas dissolves in the liquid around the bubble. In addition, a part of the steam condenses on the bubble interior wall and returns to a liquid. However, many gas molecules and a quantity of steam remain because of the constrictive speed of the bubble. Therefore, the pressure in the bubble continues to rise. The high rate of shrinkage of the bubble also causes heat generated by the shrinkage, and transmitted to neighboring liquids by outward flow from the air bubble interior, increasing the thermal energy of the bubble. This represents the adiabatic process that occurs in conjunction with so-called insulated compression. The temperature in the bubble increases and the pressure p_g also rises.

The value of p_g increases especially rapidly, from 10 to 100 MPa, as the bubble is compressed and the internal density eventually matches that of the surrounding liquid. As a result, term 2 on the right side of Eq. (14) increases and the acceleration of the air bubble wall takes on a large positive value such that the air bubble shrinkage ceases. At this point, the temperature in the bubble can exceed several thousand K.

The cavitation resulting from low flow pressure has a size of more than 100 μm, a value that is larger than that associated with ultrasonic cavitation, since the size of the inner part of the bubble is limited by the vapor pressure of the water. It is a characteristic of this cavitation collapse pressure that it is larger than that associated with ultrasonic cavitation. The cavitation generated by low flow pressure and circulation is associated with expansion and shrinkage, leading to multifunction cavitation. Multifunction cavitation involves larger bubbles with higher temperatures and pressures than those generated during conventional cavitation processes, increasing the work ratio of the microjets.

The mechanism described above transitions floating cavitation to the multifunction cavitation process in which hot spots are generated. This multifunction cavitation is applied to the solid surface as soon as the cavitation starts to collapse, and the associated decrease in the cavitation volume in conjunction with the high velocity waterjet generates a so-called microjet, just as in conventional cavitation. Because the microjet in this new process is capable of both mechanical and electrochemical action, it can generate changes in both surface morphology and chemical characteristics of the material being treated. Thus, multifunction cavitation is anticipated to have applications in various industrial fields, including photocatalysis, clean energy, medical care, chemistry, and engineering.

2.6. Ultra-high temperature and pressure cavitation

In order to generate the high-temperature and high-pressure cavitation, the effect of placing an additional nozzle on a waterjet nozzle is evaluated experimentally and theoretically. Instead of

http://dx.doi.org/10.5772/intechopen.79530

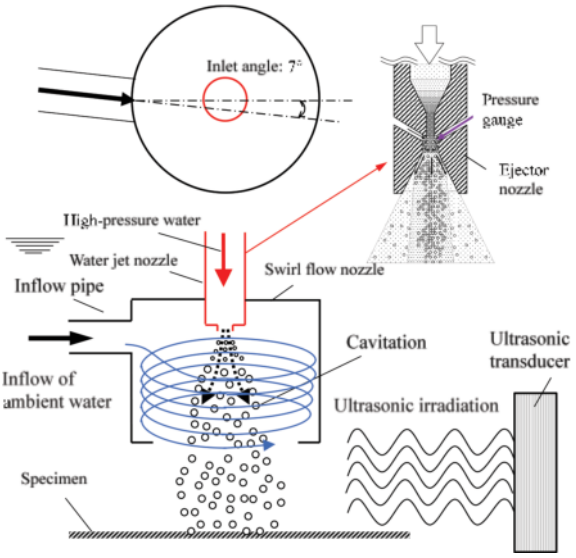

Figure 3. Generation of high-temperature and high-pressure cavitation by swirling straight nozzle (inflow hole: 1 piece).

a waterjet nozzle, the ejector nozzle is attached to the additional nozzle to measure the static pressure around the exit point of the waterjet nozzle, as shown in **Figure 3** [11] and **Figure 4**.

The static pressure at the exit of waterjet nozzle decreases with the increase of dynamic pressure caused by high flow rete. The static pressure in case of only the waterjet nozzle, that

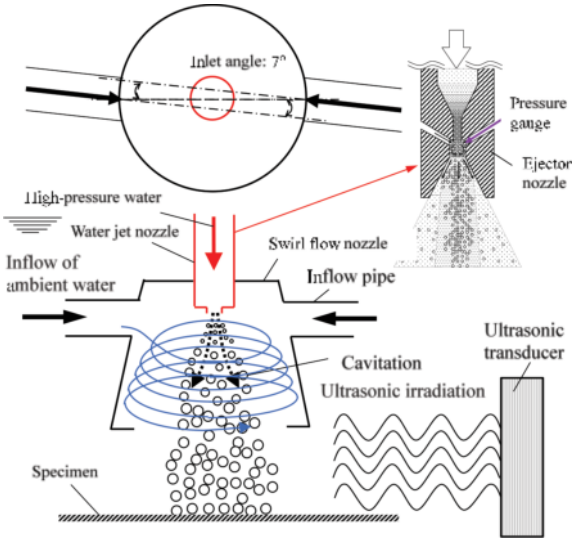

Figure 4. Generation of high-temperature and high-pressure cavitation by swirling taper nozzle (inflow hole: 2 pieces).

no additional nozzle is combined to is −8.5 kPa. On the other hand, the static pressure at the exit of ejector nozzle in the swirl flow straight nozzle shown in **Figure 1** is a high negative pressure of −36.5 kPa. The negative pressure of the swirl taper nozzle further decreases to be −47.5 kPa. The static pressure at the exit point of the waterjet nozzle decreases with the increase of dynamic pressure caused by a high flow rate. The static pressure when there is only the waterjet nozzle with no additional nozzle combined with it is −8.5 kPa. On the other hand, the static pressure at the exit point of the ejector nozzle in the swirl flow straight nozzle shown in **Figure 1** has a high negative pressure of −36.5 kPa. The negative pressure of the swirl taper nozzle further decreases to −47.5 kPa.

In a swirl flow straight nozzle and a swirl flow taper nozzle, the surrounding water enters through the inflow pipe and the swirl flow occurs due to the static pressure decreasing at the exit point of the waterjet nozzle. When the inflow hole is closed, the static pressure at the nozzle outlet portion is −3 kPa, and the negative pressure becomes smaller than −6 kPa when the swirl nozzle is not attached. This is probably because the supply of ambient water is restricted as compared to when there is no additional nozzle, so the fluid pressure in the swirling nozzle increases, the inflow of high pressure water decreases, and the dynamic pressure at the outlet decreases.

The discharge pressure of the high-pressure pump used in this experiment was 35 MPa and the flow rate was 15 L/min, but when a waterjet nozzle with a nozzle diameter of ϕ0.8 mm was used, the measured value of the flow rate was 6.9 L/min. The flow velocity of nozzle discharge obtained from the nozzle sectional area is 229 m/s.

An increase in the number of occurrences of cavitation due to a swirling flow in the nozzle and a pressure required for bubble expansion are obtained. When the internal pressure p_n of the swirling nozzle becomes negative, the flow velocity v_i in the inflow hole can be obtained by Eq. (16). Here, the pressure p_i at the entrance of the inflow hole is set to atmospheric pressure. In practice, however, it is necessary to consider the tube inlet loss and tube friction pressure loss. The pressure loss is expressed by Eq. (17), the actual pipe flow rate u is expressed by Eq. (18), and the flow rate Q is expressed by Eq. (19), with the pipe inlet loss coefficient ζ being 0.5 and the tube friction coefficient λ being 0.03.

$$p_n = p_i - \frac{\rho}{2} {v_i}^2 \tag{16}$$

$$\frac{1}{2} {v_i}^2 = \zeta_{in} \frac{u^2}{2} + \lambda \frac{l}{d} \frac{u^2}{2} \tag{17}$$

Here, the inlet loss coefficient ζ in: 0.5, the pipe friction coefficient λ: 0.03, d: pipe inner diameter (20 mm)

$$u = \sqrt{\frac{{v_i}^2}{1 + \zeta_{in} + \lambda \frac{l}{d}}} \tag{18}$$

$$\mathrm{Q} = \frac{\pi}{4} d^2 u \tag{19}$$

http://dx.doi.org/10.5772/intechopen.79530

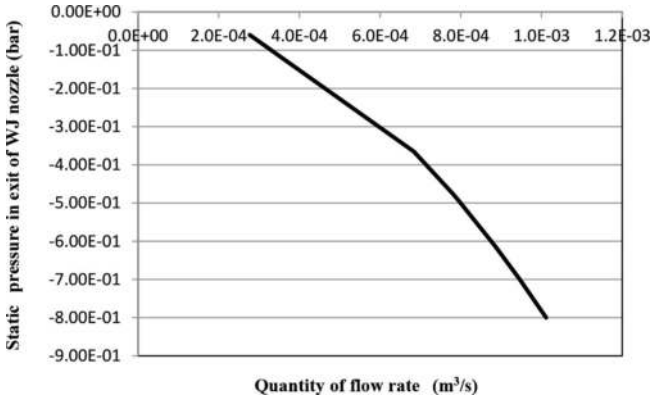

Figure 5. Flow rate in inflow hole and pressure in swirling nozzle.

The relationship between the pressure p_n at the outlet of the waterjet nozzle and the flow velocity u within the pipe and the relationship between the pressure p_n at the outlet of the waterjet nozzle and the flow rate Q within the pipe are shown in **Figures 5** and **6**, respectively. As shown in **Figures 5** and **6**, the flow rate was 6.83×10^{-4} m^3/s and the flow rate was 2.17 m/s at the swirling straight nozzle (one inflow hole) having a pressure of −36.5 kPa at the outlet of the waterjet nozzle, and the waterjet had a flow rate of 7.79×10^{-4} m^3/s and flow velocity of 2.48 m/s in the swirling taper nozzle (2 inflow holes) with the nozzle outlet pressure of −47.5 kPa.

After entering at 7°, a swirling flow is formed, but it was assumed that the inner wall of 64 mm of the SFN nozzle was the earliest swirling flow. Thus, the maximum radius of the swirling flow was 32 mm, which was half of the 64 mm inner diameter of the SFN. The vortex flow that has flowed into the swirl nozzle can be treated as a circulation Γ defined by the expression (20).

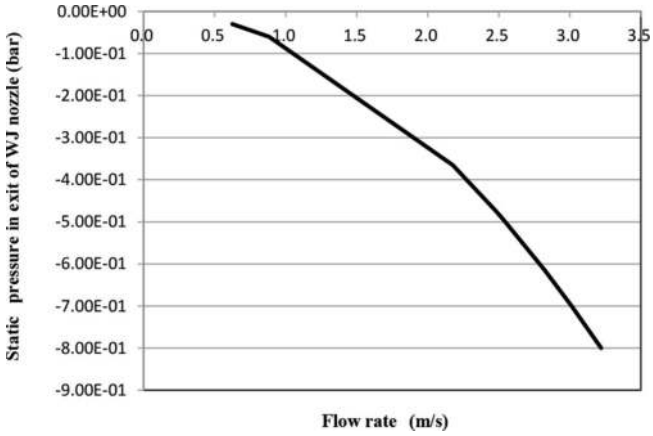

Figure 6. Relationship between flow velocity in inflow hole and pressure in swirling nozzle.

$$2\pi ru = \Gamma \tag{20}$$

Here, the circulation of the bubble nucleus is Γ, r_c = 0, the pressure at the center is p_m, the pressure in the swirl nozzle is p_n, and the circulation radius is r. An arbitrary pressure p in the vortex is given by Eq. (21).

$$p = p_n - \frac{\rho u^2}{2} \tag{21}$$

However, with the actual vortex, this state cannot be continued to the center, and it forms the core part corresponding to the strength of the vortex. Inside the nucleus, the value of the circulation is not constant and varies according to Eq. (22) by the radial position r_c.

$$2\pi r_1 \left(u \frac{r_1}{r_c} \right) = \Gamma \tag{22}$$

Considering the flow in this swirl nozzle, the radius r_1 of the nucleus is determined as the turning radius obtained from the position of the inflow hole. The circulation Γ increases as the inflow velocity increases and the pressure p_m of the swirl center (nucleus center) is further reduced as compared with the nozzle exit pressure p_n as shown in the Eq. (23).

$$p_m = p_n - \frac{\rho \Gamma^2}{4\pi^2 {r_1}^2} \tag{23}$$

It is considered that the negative pressure increases from the one-hole swirling straight nozzle to the two-hole taper nozzle, as shown in **Figure 7**.

Cavitation number is a dimensionless number used for analysis of cavitation in hydrodynamics. It is mainly used for analyzing fluid machinery using a liquid such as a pump, water piping, and hydraulic equipment. The cavitation number Ca is defined as a dimensionless version of the difference between the pressure of the liquid and the vapor pressure, and is expressed by Eq. (24),

$$c_a = \frac{p_m - p_v}{(1/2)\rho {v_n}^2} \tag{24}$$

where p_m is the absolute pressure, p_v is the vapor pressure (20°C), $(1/2)\rho {v_n}^2$ is the representative pressure (dynamic pressure), ρ is the fluid density, and v_n is the representative velocity of the flow (swirl center flow velocity).

Ca = 1 at the cavitation generation point, and when Ca < 1, cavitation occurs in this piping system. The smaller the cavitation number, the more easily cavitation occurs. The faster the representative speed of flow, the easier the cavitation occurs. Generally, when the temperature is high, the vapor pressure rises, so cavitation tends to occur.

In this study, the flow velocity from the nozzle exit is estimated from the spreading of the free jet from the waterjet nozzle, and **Figure 8** is obtained when the cavitation number is obtained.

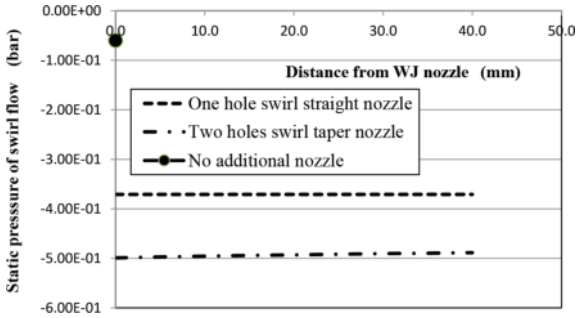

Figure 7. Relationship between distance from the waterjet nozzle and swing center pressure.

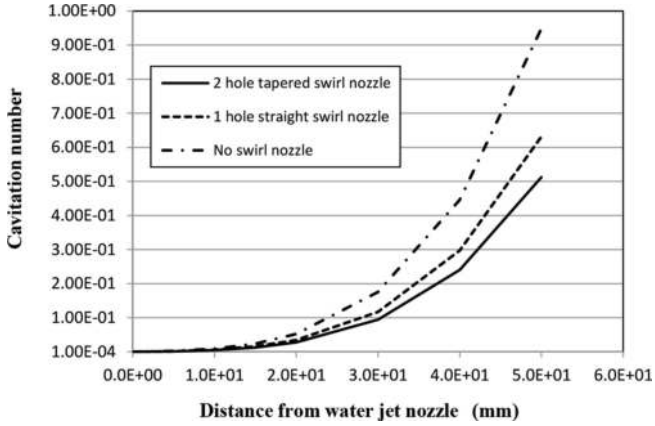

Figure 8. Relationship between the distance from the waterjet nozzle and cavitation number.

Compared with the case when there are no additional nozzles, it can be seen that the number of cavitation increases for a one-turn swirl straight nozzle, and furthermore that the two-hole swirling taper nozzle tends to generate more cavitation bubbles. As a result, the number of waterjet bubbles flowing out of the additional nozzle and being irradiated with ultrasonic waves increases, and more high-temperature and high-pressure cavitation is generated.

The liquid pressure p_B in the vicinity of the bubble wall is expressed by Eq. (25). As shown in **Figure 9**, in the case of the initial bubble radius $R_0 = 10$ μm, when the pressure (liquid pressure) around the bubble reaches a minimum value of 0.003 bar (absolute pressure) or less, the bubble can expand greatly.

$$p_B = \left(p_0 + \frac{2\sigma}{\mathrm{R0}} - p_v\right)\left(\frac{R_0}{R}\right)^{3\kappa} + p_v - \frac{2\sigma}{\mathrm{R}} \tag{25}$$

Here, p_v is the water vapor pressure, p_0 is the ambient pressure, σ is the surface tension, R_0 is the equilibrium radius, R is the bubble radius, and κ is the specific heat ratio (1–1.4). **Figure 9**

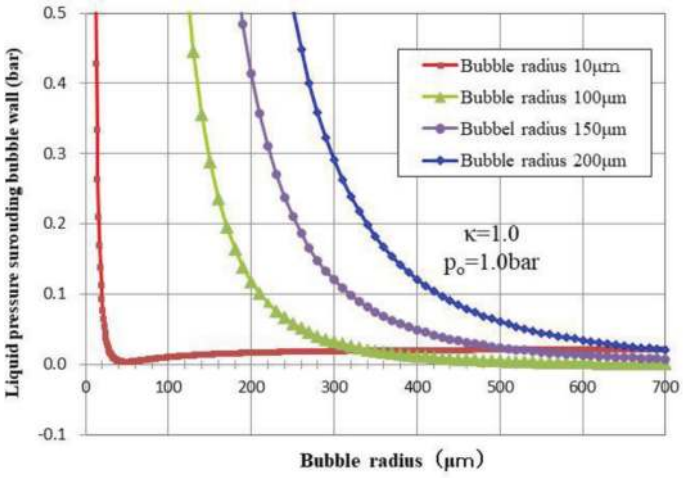

Figure 9. Relationship between bubble radius and liquid pressure near bubble wall.

shows the pressure and bubble radius of the process of bubble growth when the bubble radius is 10, 100, 150, and 200 μm at 1 atm. When the swirl flow nozzle (SFN) is used, the pressure is reduced to an absolute pressure of about 0.6 atm (dashed line), so that the bubbles increase by about 20% at each size. In addition, in the multi-bubble state, a local low-pressure region is formed due to bubble collapse. Therefore, as shown in **Figure 9**, large bubbles tend to expand with lower pressures, and when the pressure is lower than the critical pressure, the bubbles expand greatly. The addition of a negative sound pressure, such as by irradiation with ultrasonic waves, is required to reduce the pressure below the critical pressure. As described above, the swirl flow nozzle rapidly expands the numerous bubbles produced by the WJC. As a result, bubbles flowing out of the swirl flow nozzle produce ultra-high-pressure cavitation.

Further, when the swirl flow nozzle is tapered, the circulation radius gradually increases and the pressure at the circulation center decreases, so that it is possible to further increase the size of the bubble and achieve high temperature and high pressure (see **Figures 7** and **8**).

Figure 9 shows the dependence of initial bubble radius on temperature and pressure of high-temperature and high-pressure cavitation bubbles. The initial bubble radius of the conventional ultrasonic cavitation and that of the multifunction cavitation is assumed to be 4 and 100 μm, respectively. On the other hand, the initial bubble radius of the ultra-high-temperature and pressure cavitation is supposed to be 300 μm, owing to the expansion by the SFN. The isothermal expansion and adiabatic compression provides the increase in temperature and pressure. In conventional ultrasonic cavitation, the bubble pressure can be increased only to 10 MPa, but it is 1×10^5 MPa in the conventional functional cavitation and over 5×10^6 MPa in the ultra-high-temperature and high-pressure cavitation using the swirl flow nozzle. In the conventional ultrasonic cavitation, the temperature can be raised only to 3900 K, whereas the temperature increases remarkably to 1×10^8 K in the multifunction cavitation. On the other hand, in the conventional ultrasonic cavitation, the temperature can be raised only to 3900 K,

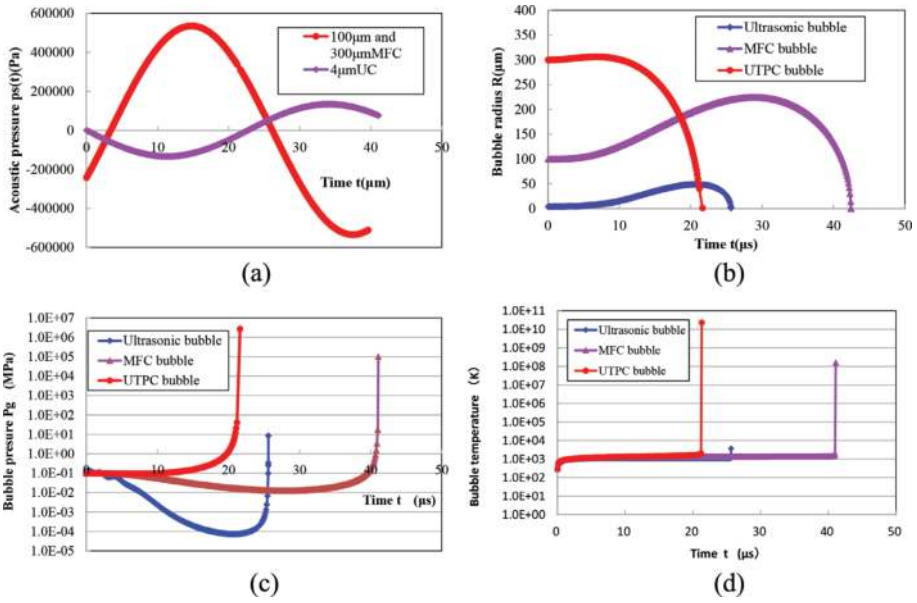

Figure 10. Dependence of initial bubble radius on temperature and pressure of high temperature and high-pressure cavitation bubbles. (a) Acoustic pressure. (b) Bubble radius. (c) Pressure inside bubble. (d) Temperature inside bubble.

whereas the temperature increases remarkably to 1×10^8 K in the multifunction cavitation. The bubble temperature of 1×10^{10} K is obtained in the super-high-temperature and high-pressure cavitation using the SFN. However, in fact, at the final stage of contraction, although the increase in the bubble temperature is suppressed by chemical reaction heat and heat conduction accompanying the thermal decomposition of steam, it is handled as a qualitative comparison in the calculation formula. In conventional measurement data of sonoluminescence, it is considered that the maximum bubble temperature is 100,000 K, and it is considered that this temperature has been reached in this calculation (**Figure 10**).

3. Experimental

Previously, we developed an ejector nozzle that can produce mechanochemical cavitation. As shown in **Figure 11**, sub-stream suction occurs in small-sized high-pressure ejector nozzles because the dynamic pressure of the high-pressure water in the nozzle can increase. Moreover, the sub-stream contains water, TiO_2 particles, and Pt particles mixed with the high-pressure water. In the ejector nozzle, the generation, growth, and collapse of cavitation are repeatedly applied to the surfaces of the titanium oxide and platinum particles. Because the cavitation has an extremely high collapse pressure, the surfaces of the titanium oxide and platinum particles are processed by the cavitation microjets in the ejector nozzle reactor. The surface area of the titanium oxide and platinum particles should increase, which would lead to the increment of

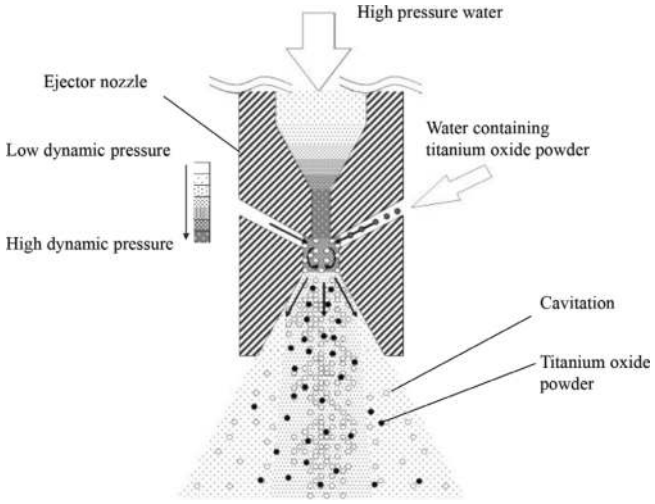

Figure 11. Cavitation processing of a photocatalyst powder by the ejector reactor.

reaction activation point and improved photocatalysis. For comparison with the cavitation processed powder, titanium oxide particles and mixed titanium oxide and platinum particles were immersed in water and stirred with a magnetic stirrer. This represents a more conventional approach, in which TiO_2 and Pt particles undergo simple mixing in solution via a magnetic stirring mechanism [16]. Generally, the Pt or other co-catalyst is added to TiO_2 in a concentration range of 0.1–1.0 wt% when investigating photocatalytic properties [17], and it has been reported that a Pt content of 0.75 wt% in Pt-TiO_2 produces the best photocatalytic performance [18]. However, since it was anticipated that some of the Pt in the sub-stream would be lost during the Ejector Cavitation (EC) processing, a TiO_2 to Pt ratio of 10:1, which corresponds to 9.1 wt% Pt, was also employed for comparison. In order to compare the results of EC processing with the results obtained by processing with simple ultrasonic cavitation, a TiO_2–9.1 wt% Pt (1 μm) particle mixture was suspended in water and subjected to ultrasonic irradiation for 30 min. In these trials, the frequency of the ultrasonic waves was 38 kHz and the power output was 100 W. The particles processed via EC, ultrasonic cavitation and simple stirring were all collected by heating the solutions to evaporate the water.

Titanium oxide may adopt three different crystal structures, each with the chemical formula TiO_2. The first is rutile-type, the second is anatase-type and the third is brookite-type. The anatase-type and the rutile-type are typically used in photocatalysis studies. The anatase-type has better photocatalytic properties than the rutile-type, although the rutile-type tends to absorb light with longer wavelengths (closer to visible light) than the anatase-type. The rutile-type TiO_2 used for experimental trials was obtained by the chlorine method (also known as the gas phase method). The TiO_2 content of the resulting material was 99.997%, the average particle size ranged from 200 to 300 nm, the rutilation coefficient was 100% as measured by X-ray diffraction, and the specific surface area was 6.57 as assessed by the BET method. The anatase-type TiO_2 employed in this work was TIPAQUE® A-100, synthesized by the sulfuric

acid method (the liquid phase method). A-100 is small-particle, sulfate-processed anatase that exhibits greater brightness and a more bluish color tone than rutile. The non-surface treated product is less durable, but has good self-cleaning properties and is sufficiently versatile that it can be used in cosmetics as well as industrial-type applications such as plastics, rubber and traffic paints. The average particle size of the material was 160 nm, the TiO_2 content was 98%, its oil absorption was 22/100 g and its pH ranged from 6.5 to 8.0. The platinum particles were greater than 99.0% pure and had a bulk density of 3.80 g/cm^{3,} a specific surface area of 20.99 (as measured by the BET method), and a loss on drying of 0.29% on heating to 80°C.

Figure 12 shows the equipment used to measure the photocatalytic properties of titanium powders. The cavitation processed particles and the stirred particles were placed on a quartz glass sample stand, and the chamber was exhausted by a turbomolecular pump to a vacuum level of 5×10^{-4} Pa. The total pressure was measured by an ionization gauge. The position of the specimen was controlled by the feedthrough motion of magnet coupling. Monochromatic UV light from a xenon lamp source with a wavelength of 365 nm and a power density of 4000 mW/cm^2 was irradiated onto the specimen through a quartz glass viewport. The total amount of UV energy ranged from approximately 200–400 mW, and the focal distance of the lens was 120 mm. The gas generated from the TiO_2 surface under ultraviolet irradiation was measured by quadrupole mass spectrometry (QMS). In the initial 20 seconds of these measurements, the quadrupole mass spectrometry was performed without the ultraviolet irradiation. Then, ultraviolet irradiation and the mass spectrometry were both applied to the specimen for the next 20 seconds. Finally, the irradiation was stopped while the quadrupole mass spectrometry continued for another 20 seconds. Furthermore, LED device emitting light ranging from 400 to 800 nm and having a power density of 100 mW/cm^2 was used to generate simulated sunlight and this light was applied to the test specimen through a quartz glass viewport. The gases generated from the TiO_2 surface under visible light irradiation were quantified by

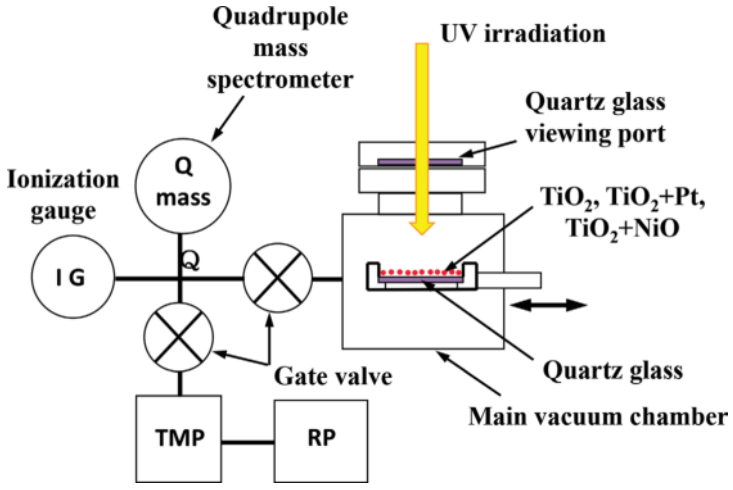

Figure 12. Schematic of equipment used in the present photocatalytic experiments.

quadrupole mass spectrometry. In the initial 20 seconds of each trial, the quadrupole mass spectrometer was operated without applying visible light irradiation, after which visible light irradiation was applied to the specimen until hydrogen and oxygen generation was detected based on their respective peaks.

The specimen produced by ejector cavitation processing (as shown in **Figure 11**) did not generate hydrogen through water splitting in response to visible light irradiation, whereas hydrogen generation did occur upon UV irradiation. This can be explained by noting that the energy of UV light is greater than that of visible light. Because the band gap associated with water splitting by the photocatalyst is in the range 3.0–3.2 eV, the generation of holes in the valence band and the movement of electrons to the conduction band are both difficult when the increased reaction points are generated only by nanolevel ejector processing. As noted, multifunction cavitation results in both mechanical and electrochemical processing by the microjet as a consequence of the presence of hotspots and their chemical reaction field. Therefore, reductions in the band gap and the promotion of water splitting would be expected. In present study, the surface potential images of titanium oxide particles was measured by KFM (Kelvin Probe Force Microscope).

A Kelvin force microscope (KFM) was used to measure surface potential. A KFM observes specimen morphology and potential by variations in the work function and the contact potential. "Work function" is the energy required in order to extract a single electron from the surface of the substance, or, in other words, how easy it is to extract hydrogen. This is diagrammed in **Figure 13**.

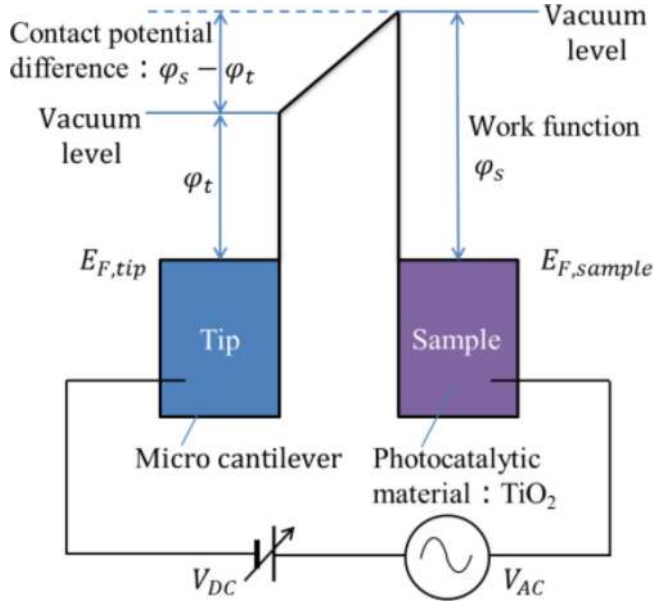

Figure 13. Schematic diagram of the Kelvin force microscope.

http://dx.doi.org/10.5772/intechopen.79530

4. Results and discussion

Chemical reactions of the ITO film on the soda-lime glass can also be induced by multifunction cavitation, as shown in **Figure 14**. The ITO film is composed of In_2O_3 and SnO_2 and its melting point is in the range of 1800–2200 K, while the soda-lime glass on which the ITO film is deposited has a melting point of 1270 K and is made from a mixture of SO_2, Na_2CO_3, and $CaCO_3$. The microjet hot spots were found to peel the ITO film from the glass to generate particles consisting of a combination of the ITO film and the soda-lime glass.

Figure 15 presents a surface FE-SEM image of TiO_2 particles supporting minute Pt particles after EC processing. Nanoscale roughness was formed on the surface of the TiO_2 particles after the cavitation processing. The pressure of cavitation collapse was estimated to be approximately 1000 MPa. It is considered that the titanium surface was processed by the micro-jet of cavitation, when the cavitation approaches to the surface of the titanium particles in the ejector reactor. Because the exit of the ejector nozzle is narrow and has a small gap, the particles are very likely to encounter the cavitation and suffer the micro-jet fabrication in the ejector nozzle. Because the specific surface area of the titanium oxide particles increases, the reaction activation point changes, and the amount of gases generated should increase under ultraviolet irradiation.

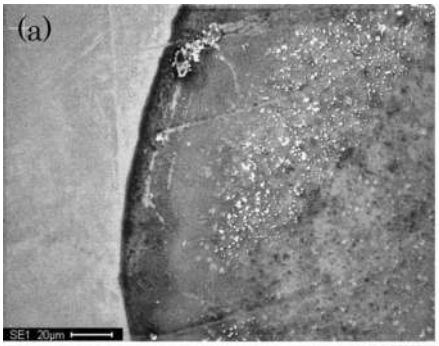

Element	*Wt%*	*At%*
CK	8.86	16.16
NK	6.34	9.91
OK	26.12	35.74
NaK	6.65	6.33
MgK	2.36	2.13
AlK	0.96	0.78
SiK	30.39	23.69
InL	13.33	2.54
CaK	4.98	2.72
Matrix	Correction	ZAF

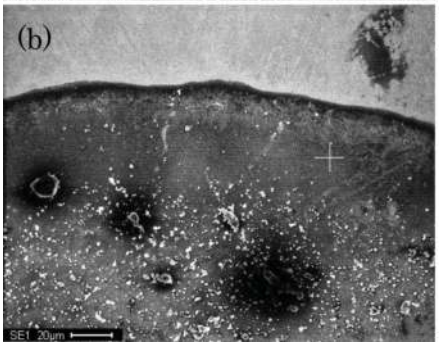

Element	*Wt%*	*At%*
CK	23.02	36.59
NK	5.31	7.24
OK	24.87	29.68
NaK	4.54	3.77
MgK	1.60	1.26
AlK	0.96	0.68
SiK	24.84	16.88
InL	10.27	1.71
CaK	4.60	2.19
Matrix	Correction	ZAF

Figure 14. Chemical reactions of an ITO film on soda-lime glass following multifunction cavitation (a) region at which the ITO film was not removed; (b) region at which the ITO film was removed.

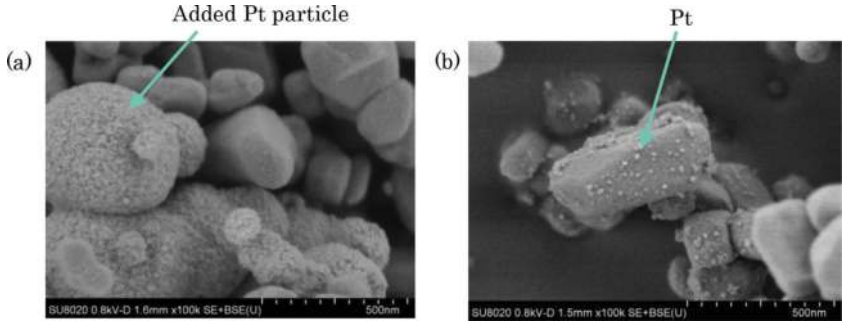

Figure 15. FE-SEM images of TiO_2 particles supported by Pt particles as a co-catalyst after cavitation processing (×100,000). (a) Pt particle mixed with TiO_2 and (b) minute Pt particles supporting TiO_2 particles.

The Pt nanoparticles were detached from the surfaces of the original Pt particles and attached to the surfaces of the TiO_2 particles, as shown in **Figure 15**. Such nanoparticles are thought to act as a co-catalyst to promote the photocatalytic reaction. Conventionally, Pt addition is performed using an electrodeposition method [16], in which Pt becomes attached to the titanium oxide surface by stirring Pt and TiO_2 particles in a methanol/water solution under UV irradiation for about 40 hours [16]. In contrast, it takes only a few seconds to add Pt nanoparticles to the titanium oxide surface in case of EC processing. Thus, EC processing is an effective method not only for nanoscale surface processing but also for supporting one substance on another.

After treating the mixture of TiO_2 and Pt particles with multifunction cavitation, nanoscale TiO_2 particles were obtained and were found to agglomerate to produce porous structures, as shown in **Figure 16**. The microjets resulting from floating cavitation of the waterjet were not able to fabricate nanoscale TiO_2 particles such as these. In addition, the hot work performed by the microjet hot spots tended to melt the TiO_2 particles. It should be noted that Pt co-catalyst particles were also generated during the multifunction cavitation process and were intermingled with the molten, porous TiO_2.

It may be premature to expect that surface treatment by micro-jet can enhance the photocatalytic properties in emulsified water under visible light. However, the bandgap of rutile-type TiO_2

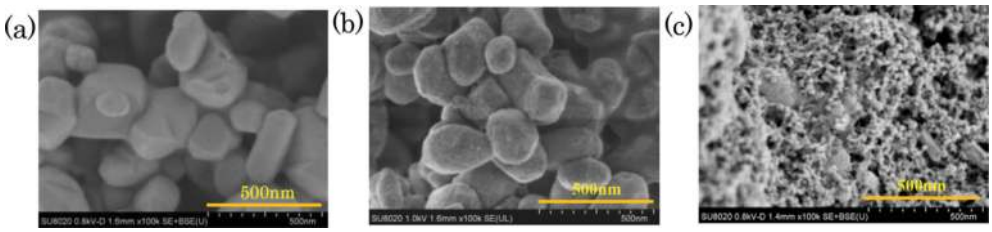

Figure 16. FE-SEM images of titanium oxide particles (a) as-received, (b) after WJ processing, (c) after MFC processing (×100,000).

is 3.0 eV at a wavelength of 413 nm, whereas the bandgap of anatase-type TiO_2 is 3.2 eV at a wavelength of 388 nm. In this study, a mechanical cavitation jet was used for surface processing in an ejector reactor. If the sub-stream contains not only TiO_2 but also Pt but also a chemical, mechanochemical cavitation is generated. This mechanochemical cavitation has a synergy of mechanical processing and chemical processing in the study of ballast water treatment [19, 20] and in the study of improvement of corrosion resistance. The bandgap water splitting should be decreased by the processing of mechanochemical cavitation.

When water is irradiated with ultrasound, acoustic cavitation occurs with the concurrent generation of active oxygen species and shock waves [21–23]. Previously, the use of ultrasound was investigated for disaggregation of agglomerated particles and surface modification of diamond nanoparticles [24]. Coating of host particles with guest nanoparticles by ultrasonic irradiation in liquid CO_2 has also been studied [25, 26], as well as mixing and conjugation of nanoparticles using ultrasonic cavitation in high-pressure liquid CO_2 [27, 28]. Sonodynamic therapy was applied to cancer cells based on the delivery of titanium oxide (TiO_2) nanoparticles modified with avidin protein, which preferentially discriminated cancerous cells from healthy cells [29]. **Figure 18** compares the amount of hydrogen, oxygen and water generated from EC-processed, ultrasonic cavitation (UC)-processed and stir-processed TiO_2 particles supporting Pt (TiO_2 + 9.1 wt% Pt). It can be seen that gas generation for the UC-processed particles is less than that for the EC-processed material. In this study, the EC processing technique was investigated with the aim of obtaining a new photocatalytic material, and it was shown to represent a potentially useful approach to nanoscale surface processing and synthesis of hybrids of different particles, with applications not only in the field of photocatalysis but also other industrial processes (**Figure 17**).

It was found that the work ratio generated by multifunction cavitation could be varied by tuning the pressure and processing duration as well as the power and frequency of the ultrasonic wave. The balance between hot treatment by hot spots in the microjet and high pressure physical working by the microjet is thus determined by both the waterjet and

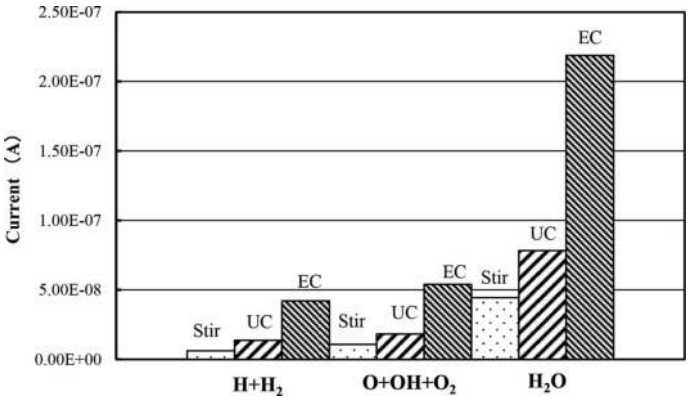

Figure 17. Comparison of EC processing, UC processing and stir processing with regard to amount of gas generation from TiO_2 particles supporting Pt (TiO_2 + 9.1 wt% Pt) under UV irradiation.

ultrasonication parameters. In the case of TiO_2, the highest work ratio was obtained when applying a waterjet pressure of 35 MPa together with a duration of 2 min, an ultrasonication power in the range of 150–300 W (ideally 225 W) and frequencies of 28, 40, and 100 kHz (with 28 kHz being optimal).

Figure 18 shows FE-SEM image and elemental maps for TiO_2 particles supporting Pt particles and other compounds produced by processing with multifunction cavitation. As noted, the TiO_2 powder was 99.997% pure and the Pt powder was more than 99.0% pure. Therefore, both materials contained low levels of impurities such as Al, Fe, Si, Na, Mg, and S. In the high

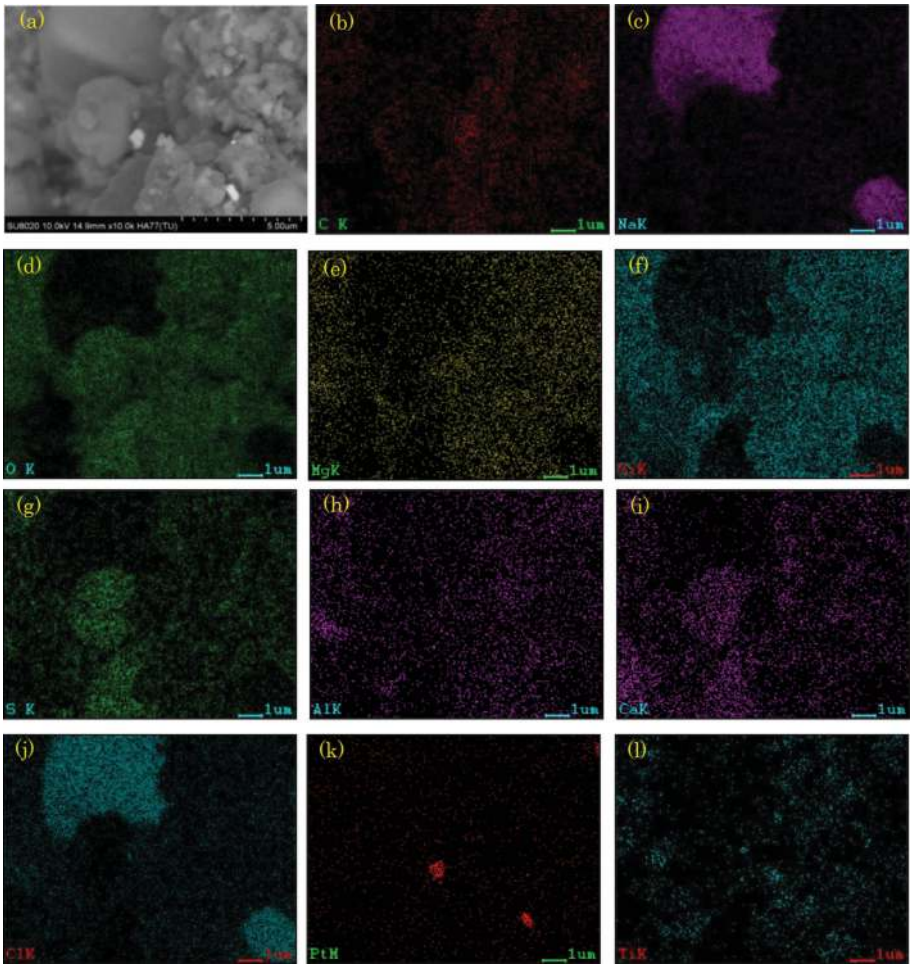

Figure 18. (a) FE-SEM image and elemental maps of (l) Ti, (k) Pt, and (d) O for TiO_2 particles supporting Pt particles and other compounds of (b) C, (c) Na, (e) Mg, (f) Si, (g) S, (h) Al, (i) Ca, (j) Cl, produced by processing with multifunction cavitation.

potential reaction field of multifunction cavitation, these impurities will gather locally in the porous structure of the TiO_2. In fact, NaCl crystals can be observed in **Figure 16**.

Figure 19 demonstrates the enhanced visible light photocatalytic properties obtained by processing with multifunction cavitation. The levels of hydrogen and oxygen that were generated following multifunction cavitation were greatly increased compared to the quantities obtained from material treated with standard waterjet processing. Interestingly, even the waterjet processing was more effective than the conventional approach, in which TiO_2 and Pt particles undergo simple mixing in solution via a magnetic stirring mechanism. It should be noted that the quantities of hydrogen and oxygen produced by water splitting under visible light irradiation were in accordance with the expected stoichiometric ratio, indicating efficient photocatalysis.

As experiments showing the effectiveness of MFC, experimental results of WJC processing, UC processing, UC processing after WJC processing, and WJC processing after UC processing were compared (**Figures 20** and **21**) [30].

A significant increase in the amount of hydrogen generation by MFC processing compared to the other processing indicates that high-temperature and high-pressure microjet is generated, suggesting an increase in the water splitting reaction point due to the increase in surface area. It can also be realized from **Figure 17(b)** and **(c)**. In addition, there is a high possibility that the band gap of water splitting by MFC treatment was reduced. Compared with other treatment methods, the amount of hydrogen generation dramatically increased in MFC treatment, and it became clear that microjet with hot spot is effective for water splitting. Also from the result of oxygen generation shown in **Figure 19**, it was confirmed that the amount of oxygen generation dramatically increased by MFC treatment as well.

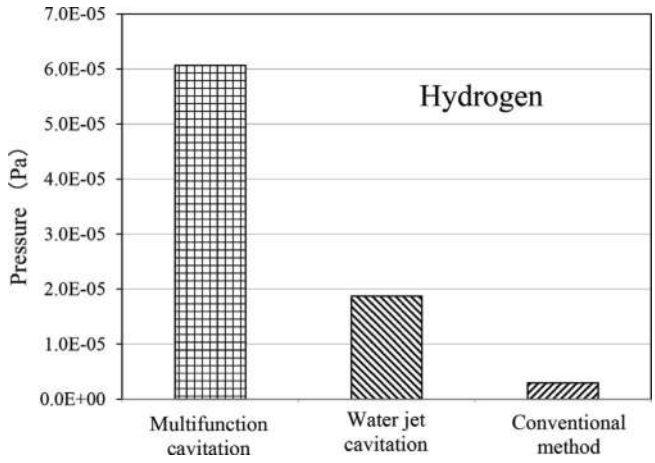

Figure 19. Visible light photocatalytic generation of hydrogen by TiO_2 following processing by multifunction cavitation or waterjet cavitation.

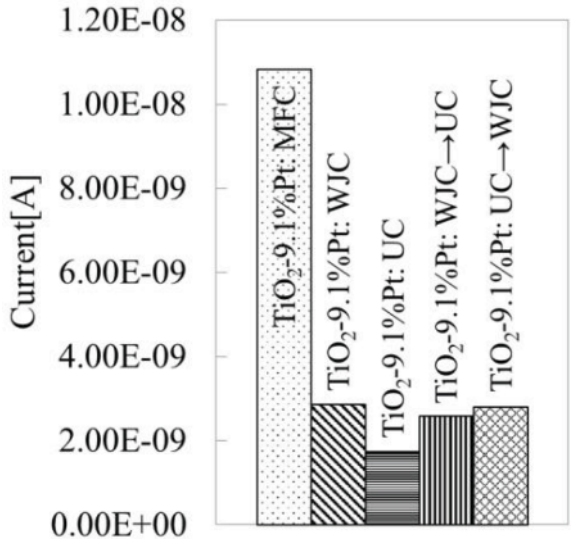

Figure 20. Hydrogen generation from various cavitation processed TiO_2 particles supported by Pt particles.

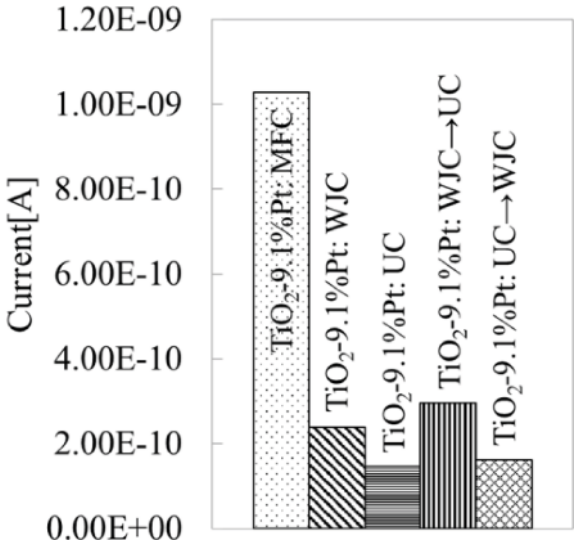

Figure 21. Oxygen generation from various cavitation processed TiO_2 particles supported by Pt particles.

Figures 22 and **23** present the results for surface potential. **Figure 22** shows the results for rutile, and **Figure 23**, for anatase. The images on the left show the results before MFC processing, and those on the right, after processing. **Table 1** also provides the measured values of the surface potential.

http://dx.doi.org/10.5772/intechopen.79530

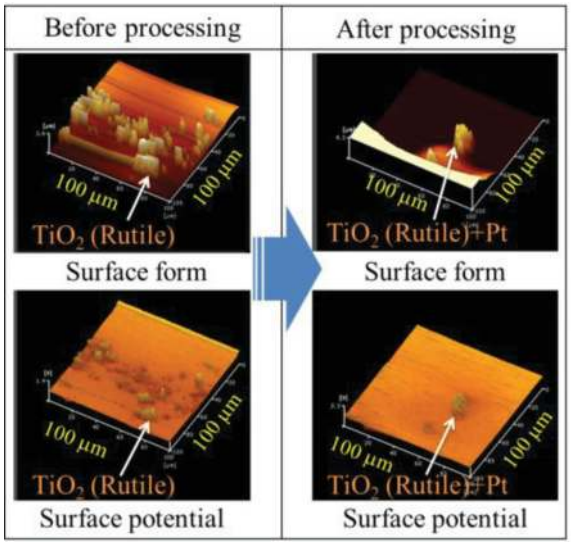

Figure 22. Results of surface potential imaging (Rutile-type TiO_2).

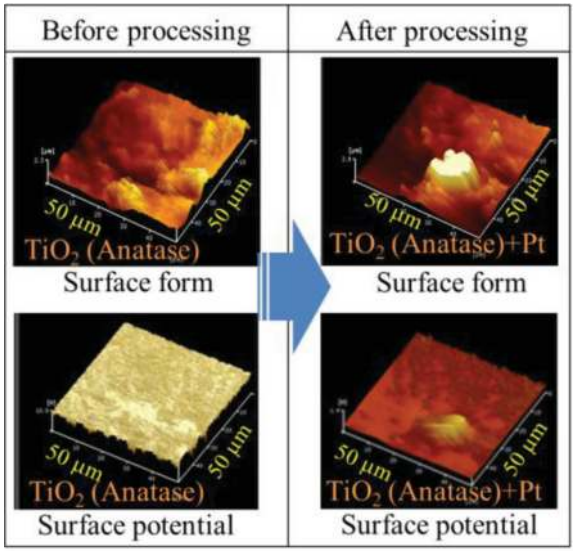

Figure 23. Results of surface potential imaging (Anatase-type TiO_2).

The results for surface potential in **Figure 23** indicate that both rutile- and anatase-type TiO_2 during processing by MFC decreases the surface potential. Also, as **Table 1** shows, for an evaluation of the surface potential of a single particle of TiO_2 powder, the mean surface

	TiO_2 type	Number	Average surface potential (V)
Before processing	Rutile	12	0.554
After processing		2	0.272
Before processing	Anatase	9	9.928
After processing		8	0.166

Table 1. Measured surface potential values.

potential of a rutile-type TiO_2 before MFC processing was 0.554 V, while it fell to 0.272 V after processing, a difference of −0.282 V in the contact potential. In anatase-type TiO_2, the mean surface potential before MFC processing was 9.928 V, but it fell to 0.166 V after processing, a difference of −9.762 V in the contact potential. The anatase-type TiO_2 showed a far higher reduction than the rutile-type TiO_2. This advantage of the anatase-type TiO_2 is consistent with its superior results in dissociation of water and with the already-known lower band gap of rutile-type TiO_2 under visible light.

Table 2 shows how the measured volume of evolved H as measured with a QMS compared with the surface potential results. In rutile-type specimens, the surface potential fell after processing, while the volume of evolved H increased. This is consistent with the promotion of H generation by the low band gap. There was also a correlation between the difference between evolved H volume and surface potential in both rutile- and anatase-type specimens. In rutile-type specimens, the surface potential fell after processing, while the volume of evolved H increased. This is consistent with the promotion of H generation by the low band gap. The particles processed by swirling taper nozzle (inflow hole: 2 pieces) of **Figure 4** further

	TiO_2: Rutile type		TiO_2: Anatase type	
	Before processing	After processing	Before processing	After processing
Surface potential (V)	0.554	0.272	9.928	0.166
$H+H_2$ Pressure (Pa)	5.28E-08	1.08E-06	-	5.81E-07

Table 2. Relationship between surface potential and $H + H_2$ pressure.

decreased to the surface potential of 0.172 V in case of rutile-type. This is a result of processing by ultra-high temperature and pressure cavitation.

5. Conclusions

After processing titanium dioxide particles and platinum particles as a co-catalyst by cavitation jet using an ejector nozzle (EC) and the multifunction cavitation (MFC), the photocatalytic performance of the modified particles under ultraviolet radiation and visible light irradiation was examined. The following results were obtained.

1. The fundamental characteristics of multifunction cavitation was assessed theoretically and experimentally.
2. In order to increase the temperature and pressure of MFC, the effect of additional swirl flow nozzle (SFN), which was put on a waterjet nozzle, was evaluated experimentally and theoretically.
3. The amount of hydrogen, oxygen, and water released from the particles was increased by EC processing.
4. Surface irregularities at the nanoscale were formed on the titanium oxide surface by EC processing.
5. TiO_2 particles were found to support Pt nanoparticles, which were detached from the original Pt particles during EC processing.
6. Materials processed by EC exhibited a higher photocatalytic performance than those processed by ultrasonic cavitation (UC).
7. The application of ultrasonication to the floating cavitation of a waterjet was found to produce microjets containing hot spots.
8. Multifunction cavitation exhibited the capacity to perform nanolevel hot working at a material surface, modifying the surface morphology and the surface electrochemical condition by hot spot melting.
9. The balance between hot treatment by hot spots in the microjet and working due to the high pressure in the microjet was determined by the waterjet and ultrasonication power conditions.
10. The amounts of hydrogen and oxygen generated by titanium dioxide particles in response to visible light was remarkably increased following treatment by multifunction cavitation compared to the results obtained following waterjet (EC) processing.
11. Doping with Pt using multifunction cavitation processing lowered the surface potential.
12. The band gap energy was also reduced concomitantly with the reduction of the surface potential, and this improved the efficiency of generation of H in the dissociation of water.

Acknowledgements

This work was supported by JSPS KAKENHI Grant Number JP24560898, JP16K06029 and was in part supported by Innovative Science and Technology Initiative for Security, ATLA.

Author details

Toshihiko Yoshimura*, Kumiko Tanaka and Masataka Ijiri

*Address all correspondence to: yoshimura-t@rs.tusy.ac.jp

Department of Mechanical Engineering, Sanyo-Onoda City University, Sanyo-Onoda, Yamaguchi, Japan

References

[1] Kling CL. A High Speed Photographic Study of Cavitation Bubble Collapse, University Michigan; 1970. Report No. 03371-2-T, 08466-7-T

[2] Yasui K. Fundamentals of acoustic cavitation and sonochemistry. In: Pankaj, Ashokkumar M, editors. Theoretical and Experimental Sonochemistry Involving Inorganic Systems. London: Springer; 2011. Chapter 1. pp. 1-29

[3] Horiuchi Y, Toyao T, Takeuchi M, Matsuoka M, Anpo M. Recent advances in visible-light-responsive photocatalysts for hydrogen production and solar energy conversion–From semiconducting TiO_2 to MOF/PCP photocatalysts. Physical Chemistry Chemical Physics. 2013;**15**:13243-13253

[4] Fujishima A, Honda K. Electrochemical photolysis of water at a semiconductor electrode. Nature. 1972;**238**:37-38

[5] Yoshimura T, Shiraishi K, Takeshima T, Komura M, Iyoda T. Nano-level surface processing of fine particles by cavitation to improve the photocatalytic properties of titanium oxide. Nanoscience & Nanotechnology-Asia. 2014;**4**:69-78

[6] Yoshimura T, Tanaka K, Yoshinaga. Development of mechanical-electrochemical cavitation technology. Journal of Jet Flow Engineering. 2016;**32**:10-17

[7] Yoshimura T, Tanaka K, Yoshinaga N. Nano-level material processing by multifunction cavitation. Nanoscience & Nanotechnology-Asia. 2018;**8**:41-54

[8] Yoshimura T, Tanaka K, Yoshinaga. Material processing by mechanical-electrochemical cavitation. In: BHR Group 2016 Water Jetting; 16–18 November 2016. University of Washington, Seattle. USA; 2016. pp. 223-235

[9] Yoshimura T, Yoshiya H, Tanaka K. Estimation of bubble fusion requirements during mechanical-electrochemical cavitation. In: BHR Group 2016 Water Jetting; 16–18 November 2016; University of Washington, Seattle. USA; 2016. pp. 327-333

[10] Ijiri M, Yoshimura T. Evolution of surface to interior microstructure of SCM435 steel after ultra-high-temperature and ultra-high-pressure cavitation processing. Journal of Materials Processing Technology. 2018;**251**:160-167

[11] Ijiri M, Shimonishi D, Nakagawa D, Yoshimura T. New water jet cavitation technology to increase number and size of cavitation bubbles and its effect on pure Al surface. International Journal of Lightweight Materials and Manufacture. 2018;**1**:12-20

[12] Gompf B, Gunther R, Nick G, Pecha R, Eisenmenger W. Resolving sonoluminescence pulse width with time-correlated single photon counting. Physical Review Letters. 1997; **79**:1405-1408

[13] Atchley AA. The Blake threshold of cavitation nucleus having a radius-dependent surface tension. The Journal of the Acoustical Society of America. 1988;**85**(1):152-157

[14] Rayleigh L. On the pressure developed in a liquid during the collapse of a spherical cavity. Philosophical Magazine. 1917;**34**(200):94-98

[15] Plesset MW. The dynamics of cavitation bubbles. Journal of Applied Mechanics. 1949;**16**: 277-282

[16] Tabata S, Nishida H, Masaki Y, Tabata K. Stoichiometric photocatalytic decomposition of pure water in Pt/TiO_2 aqueous suspension system. Catalysis Letters. 1995;**34**:245-249

[17] Kudo A. Photocatalyst materials for water splitting utilizing solar light energy. Shokubai. 2002;**44**(5):308-312

[18] Li FB, Li XZ. The enhancement of photodegradation efficiency using Pt-TiO_2 catalyst. Chemosphere. 2002;**48**(10):1103-1111

[19] Yoshimura T, Kubota S, Seo T, Sato K. Development of ballast water treatment technology by mechanochemical cavitation, In: Proceedings of the 7th International Conference on Cavitation CAV2009; 16–20 August 2009; University of Michigan, Ann Arbor. USA; 2009. Paper No. 37

[20] Yoshimura T, Motoishi M, Sato M. Study on purification of ballast water using mechanochemical-cavitation jets. Journal of Jet Flow Engineering, (The Water Jet Technology Society of Japan). 2012;**28**(3):4-11

[21] Mason TJ. Sonochemistry and sonoprocessing: The link, the trends and (probably) the future. Ultrasonics Sonochemistry. 2003;**10**:175-179

[22] Lorimer JP, Mason TJ. Some recent studies at Coventry University sonochemistry centre. Ultrasonics Sonochemistry. 1995;**2**:S79-S86

[23] Suslick KS. Sonochemistry. Science. 1990;**247**:1439

[24] Uchida T, Hamano A, Kawashima N, Takeuchi S. Improving dispersion of nanometer-size diamond particles by acoustic cavitation. Ultrasonics. 2006;**44**:473-476

[25] Matsuyama K, Mishima K. Particle coating of talc with TiO_2 nanoparticles using ultrasonic irradiation in liquid CO_2. Industrial & Engineering Chemistry Research. 2010;**49**: 1289-1296

[26] Matsuyama K, Mishima K, Kato T, Ohara K. Formation of porous glass via core/shell-structured poly(methyl methacrylate)/powder glass prepared by ultrasonic irradiation in liquid CO_2. The Journal of Supercritical Fluids. 2011;**57**:198-206

[27] Sanganwar GP, Gupta RB, Ermoline A, Scicolone JV, Dave R. Environmentally benign nanomixing by sonication in high-pressure carbon dioxide. Journal of Nanoparticle Research. 2009;**11**:405-414

[28] Sanganwar GP, Gupta RB. Nano-mixing of dipyridamole drug and excipient nanoparticles by sonication in liquid CO_2. Powder Technology. 2009;**196**:36-49

[29] Ninomiya K, Fukuda A, Ogino C, Shimizu N. Targeted sonocatalytic cancer cell injury using avidin-conjugated titanium dioxide nanoparticles. Ultrasonics Sonochemistry. 2014; **21**:1624-1628

[30] Tanaka K, Iiri M, Nakagawa D, Yoshimura T. The 9th International Conference on Leading Edge Manufacturing in 21st Century; 13–17 November 2017; Hiroshima. Japan: LEM21; 2017. Paper No. 5